

A Single-Step Bottom-up Approach for Synthesis of Highly Uniform Mie-Resonant Crystalline Semiconductor Particles at Visible Wavelengths

Mohammad Ali Eslamisaray,[†] Parker R. Wray,[†] Yeonjoo Lee, Gunnar M. Nelson, Ognjen Ilic, Harry A. Atwater,^{*} and Uwe R. Kortshagen^{*}



Cite This: *Nano Lett.* 2023, 23, 1930–1937



Read Online

ACCESS |



Metrics & More



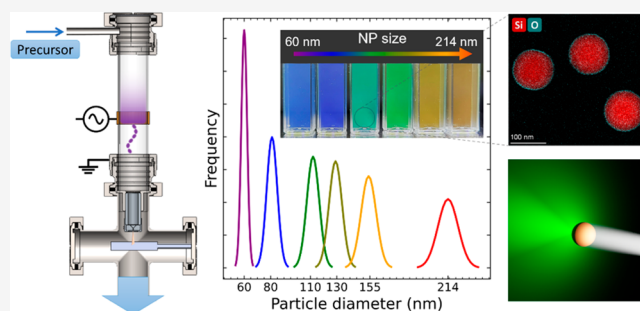
Article Recommendations



Supporting Information

ABSTRACT: Optically Mie-resonant crystalline silicon nanoparticles have long attracted interest for their unique scattering behaviors. Here, we report a bottom-up nonthermal plasma process that produces highly monodisperse particles, with diameters controllable between 60 and 214 nm, by temporarily electrostatically trapping nanoparticles inside a continuous-flow plasma reactor. The particle size is tuned by adjusting the gas residence time in the reactor. By dispersing the nanoparticles in water, optical extinction measurements indicate colloidal solutions of a particle-based metafluid in which particles support both strong magnetic and electric dipole resonances at visible wavelengths. The spectral overlap of the electric and magnetic resonances gives rise to directional Kerker scattering. The extinction measurements show excellent agreement with Mie theory, supporting the idea that the fabrication process enables particles with narrow distributions in size, shape, and composition. This single-step gas-phase process can also produce Mie-resonant nanoparticles of dielectric materials other than silicon and directly deposit them on the desired substrates.

KEYWORDS: *nanophotonics, nonthermal plasma, silicon nanoparticles, bottom-up synthesis, magnetic dipole, Kerker scattering*



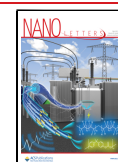
Crystalline semiconductors are an important class of materials for controlling light–matter interactions from scattering particles in the visible regime. Their interband transitions separated by a clearly defined bandgap of appropriate size can enable a large permittivity with comparatively little dissipative loss.^{1–3} This can result in a high elastic scattering efficiency, strong field localization, and scattering phenomena not accessible in other materials.^{2–8} High scattering efficiency is a direct result of inherently low absorption losses, which are particularly characteristic of indirect gap crystalline semiconductors. The scattered fields of dielectric particles are driven by displacement currents of bound charges, in contrast with plasmonic scattering, which is driven by free electron conduction currents and therefore is susceptible to Ohmic losses.^{9–11} The inherent lack of nonradiative loss implies the possibility of near unity radiative efficiency, which is important in many applications, such as extracting light from quantum emitters.¹² Similar efficiency is seen in low-index and low-loss materials, such as insulators, although this is at the expense of less field confinement, a reduced mode volume, and/or increased particle size.^{2,13,14} Alternatively, the notably large refractive index of semiconductors can produce a high scattering efficiency with strong field confinement in a low-index matrix medium.

The combination of both field confinement and low nonradiative losses can produce high-quality factor (Q-factor) resonances, and this has been shown to result in highly directional scattering.^{15–18} For example, spherical high-index and low-loss dielectric particles can exhibit strong circulating displacement currents, which mimic magnetic multipoles, termed optically induced magnetic resonances (OMRs). These artificial magnetic-type atoms are of interest in the metamaterial and metasurface community as they lead to a homogenized nonunity effective magnetic permeability at optical frequencies.^{19–21} Furthermore, these often high-Q harmonics can interfere with broadband resonances, resulting in anomalous highly directional scattering, exhibiting a Fano-like line shape, termed the Kerker effect.^{4,5,22} Unlike metals and insulators,^{2,14,23–28} indirect bandgap crystalline semiconductors can have both strong electric- and magnetic-type

Received: December 28, 2022

Revised: February 15, 2023

Published: February 23, 2023



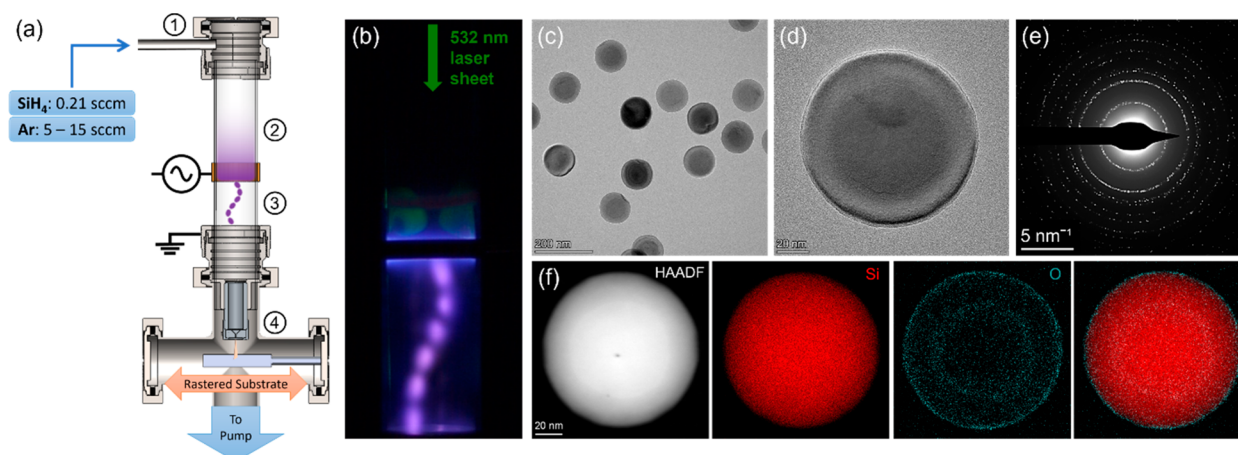


Figure 1. (a) Schematic diagram of the flow-through nonthermal plasma reactor operating in a constricted filamentary regime. (1) Precursor injection into the reactor through a side port flange. (2) Low-density diffuse region, where silane dissociation and particle nucleation begin. (3) High-density filamentary region, where size-selected particles crystallize, mainly due to electron–ion recombination heating mechanism. (4) NP extraction through the orifice and injection into the deposition chamber toward the substrates. (b) High-speed camera image of the laser light scattering experiment showing the plasma discharge (violet) and particle trapping zone (green). (c,d) Representative bright-field TEM images of c-Si NPs with a mean diameter of 112 nm. (e) SAED pattern of randomly selected Si NPs showing the crystallinity of NPs. (f) Select HAADF-STEM images of a single Si NP after air exposure for 1 day. STEM-EDX elemental maps of Si (red) and O (dark cyan) show a Si core surrounded by a thin oxide shell. Slight variations in the intensity of O within the NP might be attributed to different lattice defects, including vacancy defects, present in the c-Si NP.

Mie resonances existing simultaneously in a simple single subwavelength sphere, under plane-wave illumination.^{29–31} Furthermore, higher order electric and magnetic-type Mie resonances can also exist simultaneously in the subwavelength particle, since the large particle permittivity shrinks the effective wavelength within the particle. Crystalline semiconductors offer a platform of features desired in many fields of photonics. In that regard, spherical crystalline silicon (c-Si) particles are ideal candidates for exploring such effects in the visible region. Furthermore, c-Si particles may also integrate well with modern Si-based technologies.

Low-cost and scalable synthesis of highly uniform crystalline high-index dielectric nanoparticles (NPs), as the building blocks of metastructures and metafluids, has been a subject of active research for over a decade; however, producing ideal Si meta-atoms through bottom-up techniques still remains a challenge.³² Several fabrication methods have been developed for the synthesis of Si meta-atoms with different achievement levels over NP crystallinity, sphericity, purity, and density, as well as scalability of the technique. Femtosecond laser ablation of bulk Si donor targets in air or liquid solvents^{17,29,33–35} has been widely used to generate nanodroplets of molten Si that form into polydisperse spherical NPs upon solidification. However, the most successful laser-induced methods^{31,36,37} require complex optical systems and inherently suffer from low throughput. Gas-phase synthesis techniques enable the bottom-up production of Si meta-atoms. As one of the most promising techniques, chemical vapor deposition (CVD) can produce submicrometer-sized Si particles through decomposition of disilane or trisilane at elevated temperatures.^{38–40} Due to the larger size of the particles, their polycrystallinity, and lack of tunability over size distribution, CVD-synthesized particles have higher potential in light-scattering applications for near-IR rather than the visible spectral range. Recently, colloidal synthesis of Mie-resonant Si NPs has been accomplished by grinding Si lumps with a blender into small-sized NPs⁴¹ or thermal disproportionation of SiO

powder into Si and SiO₂ before extracting the freestanding c-Si NPs by etching out the SiO₂ matrix.^{42,43} Despite the scalability of these techniques, they require several postsynthesis processes, and their Si NPs lack either the ideal size/shape uniformity or purity.

■ PLASMA SYNTHESIS OF SIZE-CONTROLLED CRYSTALLINE SILICON NANOPARTICLES

Over the past two decades, nonthermal plasma synthesis has emerged as a competitive technology for the formation of nanocrystals that are difficult or impossible to synthesize with other fabrication techniques. Nanocrystals of covalently bonded group IV elements,^{44–46} noble and transition metals,^{47–50} and compound semiconducting materials^{51–55} are among the vast library of materials successfully synthesized by this all-gas-phase method. Nonthermal plasmas have excellent control over particle size and size distribution owing to the negative charge of the NPs immersed in the plasma, preventing particle agglomeration.⁵⁶ Compared to their liquid-phase counterparts, nonthermal plasmas also benefit from a solvent- and ligand-free process, resulting in highly pure nanocrystals in which the surface passivation could be controlled via precursor selection⁵⁷ as well as in-flight functionalization.^{58,59} By connecting the nonthermal plasma reactors to an extraction orifice, this single-step deposition technique enables the scalable collection of crystalline particles in powder form or as a thin film with tunable film thickness and porosity.⁶⁰

Despite all the promising advances, nonthermal plasmas have been long limited to synthesis of small crystalline NPs, typically <10 nm in diameter, due to the short residence time of NPs in plasma discharges. Bapat et al.⁶¹ expanded this limit to c-Si NPs of 35 nm by operating the plasma in a regime in which NPs were temporarily trapped inside the reactor. Recently, Wray et al.⁶² improved this process by optimizing the plasma conditions, pushing the average particle diameter to 82 nm with a standard deviation of 1.2 nm. In this study, we

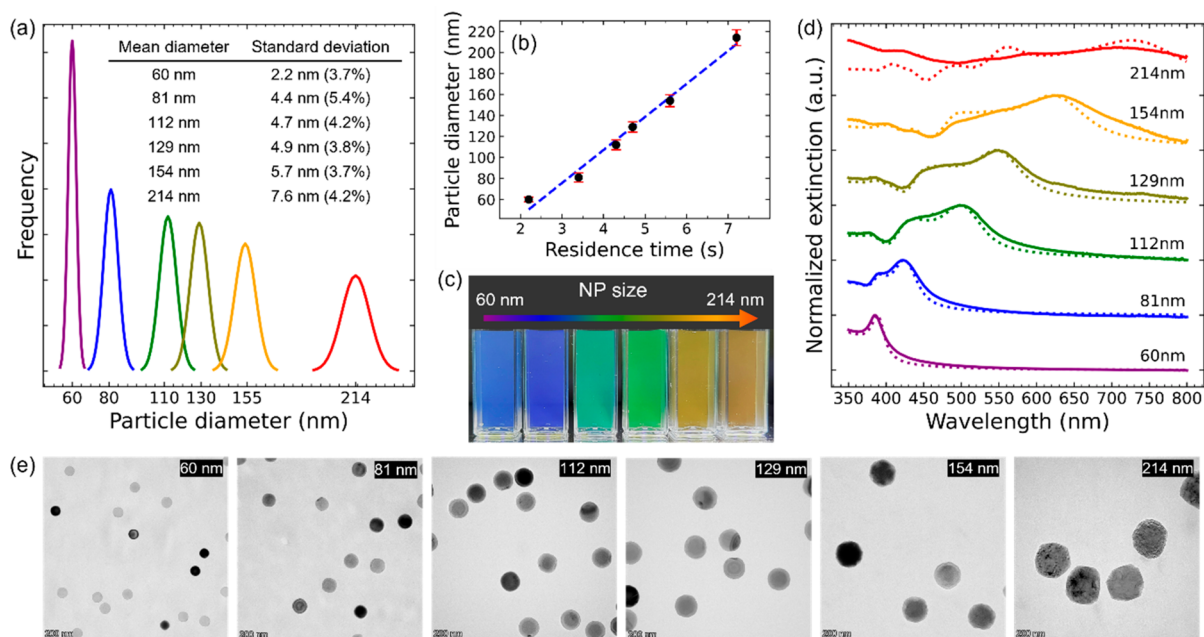


Figure 2. (a) Gaussian-fit particle size distributions, as measured by TEM analysis of hundreds of particles for each sample. Each particle size distribution is color coded from purple (60 nm) to red (214 nm). The table shows each distribution mean particle diameter, standard deviation, and percent deviation from the mean value in parentheses. (b) Average diameters of NPs as a function of the gas residence time inside the plasma reactor. Error bars are the standard deviations obtained from the particle size distribution. (c) Photographs of colloidal dispersions of monodisperse c-Si NPs in deionized water with NP size increasing from left to right. The cuvettes are illuminated with white light from the bottom. (d) Measured (solid line) and simulated (dotted line) extinction spectra of particles suspended in deionized water, (e) Representative bright-field TEM images of c-Si NPs with mean diameters ranging from 60 to 214 nm.

expand on the previous work on nonthermal plasmas that use trapping to extend the particle residence time in the reactor showing that this approach can produce monolithic c-Si NPs in a wide range of diameters exhibiting strong scattering resonance with extinction peaks covering the entire visible range.

Hydrogen-terminated c-Si NPs supporting the OMRs were synthesized via decomposition of silane (SiH_4) in a flow-through tube plasma reactor diagrammed in Figure 1a and described in detail in the Supporting Information. The precursor dissociation and particle nucleation and growth begin in a low-density diffuse plasma region upstream of the radiofrequency (RF) electrode. In this region, NPs are temporarily trapped and grow until they reach a critical size. To verify this trapping mechanism, a laser light scattering experiment was performed by shining a sheet of laser light at $\lambda = 532$ nm through the top of the reactor for *in situ* detection of trapped NPs. Figure 1b shows an image of the discharge during normal operation taken with a high-speed camera. A strong green scattering signal is observed a few centimeters above the RF electrode close to the tube wall representing a high concentration of NPs at this location. We define this region as the trapping zone. Once the desired NP size is reached, which is controlled by the gas flow rates as well as other plasma conditions, NPs are detrapped and enter the high-density plasma region downstream of the electrode. Due to the high power density in this region, the plasma is contracted into a rotating filamentary discharge channel based on a thermal-ionization instability.⁶¹ At this stage of the reactor, the NP temperature exceeds the gas temperature by several hundreds of Kelvins, mainly due to electron-ion recombination at the particle surface, resulting in crystallization of the NPs.^{61,63} The high power density in the constricted plasma region is required

for the formation of monolithic c-Si NPs because operation in a lower power diffuse regime was found to produce NPs with inferior crystallinity and morphology.

Figure 1c shows a bright-field transmission electron microscopy (TEM) image of a NP sample with a mean diameter of 112 nm. The NPs are highly uniform and spherical with minimal defects. The difference in apparent contrast of different NPs is due to the alignment of their crystallographic zone axis with respect to the electron beam, with NPs aligned with the electron beam appearing darker. The contrast difference in individual NPs, exhibiting a darker “core” and a brighter “shell”, might be attributed to crystallographic defects present in their lattice. High-resolution TEM analysis has been performed to verify that NPs are fully crystalline up to the few nm thick surface oxide layer. Figure 1d shows the TEM image of a typical NP to better emphasize the nearly complete spherical shape. The crystallinity of the NPs is further verified by the selected area electron diffraction (SAED) pattern shown in Figure 1e. Even though the focus of this article is on c-Si NPs, we also show the versatility of the nonthermal plasma technique by synthesizing germanium and silicon–germanium NPs in a similar size regime. Therefore, we show that by only changing the precursor gases flowing into the reactor we can easily switch to synthesizing other dielectrics and even their alloys (refer to the Supporting Information for more details).

Figure 2a shows six distinctly controlled c-Si NP size distributions produced using the nonthermal plasma reactor in Figure 1a. With mean diameters ranging from 60 to 214 nm, these distributions represent an over 2-fold size range produced simply by varying the gas residence time in the plasma discharge. The standard deviation of all samples is less than 5.4% of their respective mean diameters, indicating nearly monodispersed samples. Prior studies have shown that the NP

size correlates linearly with the particle residence time for plasma reactors operating in the diffuse regime.⁴⁵ The particle residence time includes two factors: (1) the time it takes for particles to travel the length of the reactor (i.e., the gas residence time) and (2) the time particles remain in the trapping zone. While the gas residence time can be easily determined, estimation of the particle trapping time requires intricate experimental methods capable of detecting individual particles in the reactor. Interestingly, recent Monte Carlo simulations of particle trapping for sub-10 nm NPs have shown that even though considering particle trapping in the reactor results in the synthesis of particles with larger sizes than the no trapping assumption, the average NP size is still linearly dependent on the gas residence time.⁶⁴ In Figure 2b, we experimentally validate this result by controlling the NP diameter in the plasma reactor via adjustment of the gas residence time. Furthermore, we show the linear relation to gas residence time holds even for particle sizes over 10× the prior studies by Monte Carlo. Therefore, NP sizes can be simply and linearly controlled in a wide size regime, despite the complex force balance in dusty plasmas. The gas residence time is defined as $t_{\text{res}} = \frac{PA_c L_p}{P_0 Q}$, where P is the pressure of the reactor, P_0

the standard pressure, Q the total gas flow rate, A_c the cross-sectional area, and L_p the length of the plasma. In Figure 2b we tuned this time between 2.2 and 7.2 s by adjusting the Ar flow rate and the orifice size while all other experimental conditions, including the silane flow rate, tube size, electrode position, and RF power, were fixed. All experimental conditions used in this study are summarized in Supporting Information Table S1.

■ OPTICAL EXTINCTION MEASUREMENTS OF SILICON NANOPARTICLE METAFUIDS

The H-terminated NPs undergo a self-limiting oxidation process upon exposure to air at ambient conditions resulting in the formation of a thin (<5 nm) oxide shell on the surface of the c-Si NPs.^{65,66} This is seen in the high-angle annular dark-field scanning transmission electron microscope (HAADF-STEM) images shown in Figure 1f. By dispersing the NPs in deionized (DI) water and sonicating the solution for 15 min, homogenized colloidal solutions are obtained. Figure 2c shows representative c-Si NPs suspended in a DI water solution under white light illumination. The samples, also termed metafluids, show a clear change in color across the visible spectrum, indicating that the size control is sufficient to produce strong and distinct Mie-resonant scattering throughout the visible. The oxide layer on the c-Si NPs is too thin to noticeably alter the resonant modes of the NPs, especially given the low index contrast between water and SiO₂. With that said, the native oxide layer at the NP surfaces does provide a negative surface charge,⁴¹ which hinders NP agglomeration in the colloidal solution.

To better characterize the unique scattering states of these NP solutions, Figure 2d shows the results of optical extinction measurements with the simulated extinction spectra overlaid. The simulated spectra, obtained through Mie theory, are based on the measured diameter distribution in Figure 2a and keep the same color convention, 60 (purple) to 214 nm (red). Apart from the 214 nm sample, we see excellent agreement between measurement and theoretical predictions in both the spectral shape and strength of the extinction. This further validates what was found in the single particle characterization in Figure 1: the nonthermal plasma process can produce, with high

accuracy and specificity, pristine c-Si particles with a nearly complete circular morphology. Size variations produced by this technique are small enough that the scattering response closely mimics that of a monodisperse particle solution (a comparison to theoretical predictions that assume a delta function particle size distribution is shown in Supporting Information). All curves are normalized as $e/\max(e)$, with e denoting the extinction, so that any potential differences in either the spectral shape or oscillator strength between measurement and theory are preserved. Therefore, the striking spectral match for sizes between 60–154 nm is not simply a result of normalizing to artificially match resonance peaks but a result of experimentally approaching near exact theoretical predictions. Both the procedure for measuring the extinction spectra and comparing measurements to simulation are described in the Supporting Information.

Figure 2e shows representative TEM images of all samples with mean diameters ranging from 60 to 214 nm. All samples are highly monodispersed, nearly completely spherical, and, apart from the 214 nm mean diameter sample which shows porous NPs, composed of fully dense c-Si. The reason behind the porosity of the NPs in the 214 nm sample is still not well understood; however, we believe that it could be due to smaller temperature variations in larger NPs within the plasma discharge. Such temperature variations, during both the heating and cooling processes, are necessary for the formation of single-crystalline, highly dense spherical NPs.^{63,67} Once dispersed in water, the pores of the 214 nm NPs are filled with water, which has a lower refractive index than Si, resulting in a reduction in the effective refractive index of the NPs. Therefore, in Figure 2d we model these water inclusions in simulation as a Bruggeman effective index and find a 20% fill fraction of water in c-Si to best fit the experimental data. All other simulated spectra assumed pure c-Si particles. More detail on the 214 nm mean diameter sample is shown in the Supporting Information.

Given the strong agreement between measurement and simulation, Figure 3 (left) takes the theoretical extinction spectra based on the measured diameter distribution and decomposes them into scattering and absorption contributions. In all cases, a strong OMR is observed. In particles around 60 nm in diameter a magnetic dipole resonance occurs at a wavelength of 375 nm. This contributes primarily to absorption-dominated spectra as this wavelength is below the visible spectrum (380–800 nm) and within the lossy region of silicon. Even in a region of appreciable loss, the large real refractive index of c-Si enables the existence of OMRs. As particle size increases, both the electric and magnetic-type harmonics red-shift and the extinction spectra become scattering dominated. Correspondingly, the radiative efficiency increases. Figure 3 (right) shows the radiative efficiency of each particle distribution. In each case, the average scattering efficiency for the spectral range starting from the peak of the electric dipole resonance to the end of the visible spectrum is reported, with minimum and maximum values shown in parentheses. The results show efficiencies approaching 99%, even though particles are clearly strongly interacting.

According to the Mie theory, the total scattering efficiency can be decomposed into electric ($\sigma_{\text{sca}}^E = \frac{1}{x^2} \sum_n \|c_n^E\|^2$) and magnetic-type ($\sigma_{\text{sca}}^M = \frac{1}{x^2} \sum_n \|c_n^M\|^2$) partial efficiencies, where c_n^E and c_n^M are the electric and magnetic-type Mie coefficients of

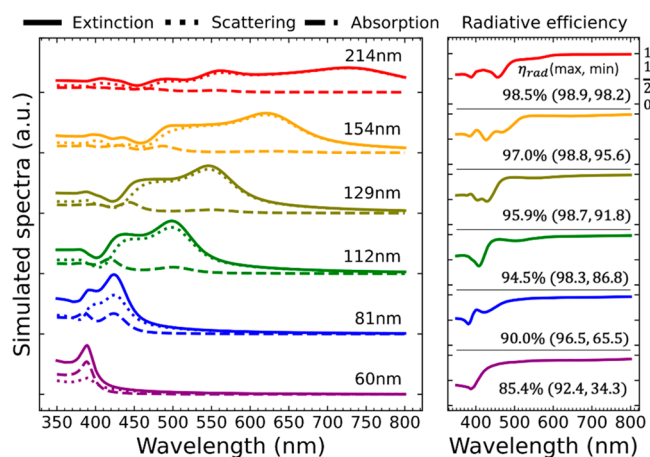


Figure 3. (Left) Simulated extinction (solid line), scattering (dotted line), and absorption (dashed line) efficiency for all particle size distributions that are shown in Figure 2a. (Right) Wavelength-resolved radiative efficiency for each particle size distribution. In both figures, all curves are color coded by mean particle size, according to the size convention in Figure 2a. The average, maximum, and minimum radiative efficiencies for each distribution are reported directly below the respective radiative efficiency curve in the right figure. These values are calculated in the spectral window, starting from the electric dipole resonance to the end of the visible spectra.

polar order, n , and $x = 2\pi r/\lambda$ is the size parameter of a particle with radius, r , at wavelength λ . The total efficiency is then $\sigma_{\text{sca}} = \sigma_{\text{sca}}^E + \sigma_{\text{sca}}^M$. The right column of Figure 4 decomposes the scattering efficiency spectra from Figure 3 into electric and magnetic type partial efficiencies to determine the fundamental atomlike oscillations that give rise to the scattering behavior. From this, we find that all particle sizes support a strong magnetic dipole resonance. Furthermore, particle sizes larger than 150 nm also support electric and magnetic quadrupoles resulting from the large and relatively lossless permittivity of c-Si. The magnetic dipole resonances are shown to spectrally intersect with the tail of the electric dipole response, a precursor to achieving Kerker scattering. To better understand the potential for anomalous directional scattering, the left column of Figure 4 decomposes the scattering spectra into a basis of directional Kerker harmonics. For spherically symmetric objects under plane wave illumination the forward (c_n^f) and backward (c_n^b) directional Kerker scattering coefficients are related to the Mie scattering coefficients through the transforms $c_n^f = \frac{(-i)^n}{2}(c_n^M - ic_n^E)$ and $c_n^b = -\frac{(i)^n}{2}(c_n^M + ic_n^E)$. The expansion into Kerker scattering coefficients simplifies the understanding of directional scattering. Some of the advantages the Kerker expansion provides include weak coupling between forward- and backward-type harmonics, clear notions of directionality and side lobes for each harmonic, and interference between the same type harmonics relating to changes in directivity. A detailed description of the Kerker harmonics is currently under review and will be published elsewhere. Under the Kerker expansion, the scattered intensity in the exact forward direction, $I(\theta = 0) = \frac{\pi}{2Zk^2} \|\sum_n \sqrt{(2n+1)} c_n^f\|^2$ is dependent only on the forward Kerker coefficients, where Z is the impedance of the host media. Likewise, the intensity in the exact backward direction,

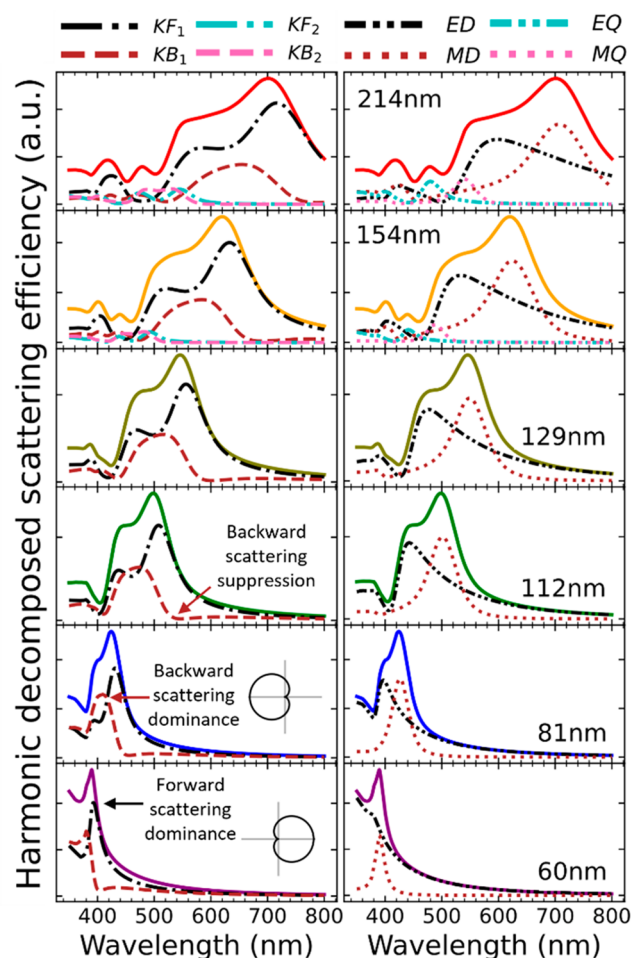


Figure 4. (Left) Decomposition of simulated scattering efficiency in terms of first (black) and second order (teal) forward (solid-dot line) and first (brown) and second order (pink) backward (dashed line) directional Kerker harmonics. (Right) Decomposition of simulated scattering efficiency in terms of first (black) and second order (teal) electric (solid-double dot line) and first (brown) and second order (pink) magnetic-type (dotted line) Mie harmonics. In both figures, the scattering spectra of each particle size distribution are color coded according to Figure 2.

$I(\theta = \pi) = \frac{\pi}{2Zk^2} \|\sum_n \sqrt{(2n+1)} c_n^b\|^2$, depends only on the backward Kerker coefficients. Furthermore, the total scattering efficiency can be decomposed into forward and backward partial powers, $\sigma_{\text{sca}} = \sigma_{\text{sca}}^f + \sigma_{\text{sca}}^b$, where $\sigma_{\text{sca}}^f = \frac{1}{x^2} \sum_n \|c_n^f\|^2$ and $\sigma_{\text{sca}}^b = \frac{1}{x^2} \sum_n \|c_n^b\|^2$. The left column of Figure 4 shows that in all size distributions there exists a spectral region characterized by anomalous directional scattering. The region near the lowest energy electric and magnetic dipole crossing shows suppressed backward coefficients and strong forward Kerker peaks. The middle electric and magnetic crossing point shows the peak in the first order backward scattering coefficient. In both the 60 and 80 nm average diameter samples we see a clear region of dominant backward Kerker coefficients, indicating anomalous backward scattering in these samples. Second-order Kerker coefficients are also seen in particle sizes larger than 150 nm.

SUMMARY

We have demonstrated the bottom-up synthesis of highly spherical pure crystalline silicon nanoparticles in the optically Mie-resonant regime using nonthermal plasmas. Particle mean diameter is controlled between 60 and 214 nm, and all samples have shown extremely narrow size distributions of less than 5.4% of their respective mean diameters. Nanoparticle size is shown to have a linear relationship with the total gas residence time in the reactor. Optical extinction measurements of NPs in water show excellent agreement with Mie theory predictions, further verifying pristine control in particle shape and material quality. Furthermore, extinction measurements show these particles exhibit both electric- and magnetic-type Mie resonances in the visible regime, giving rise to anomalous highly directional Kerker scattering. A strong magnetic dipole is seen in all samples. This is only possible due to the high degree of crystallinity of the particles, which allows for strong circular currents to exist within each particle. At present, particles with 214 nm diameter or greater exhibit a porous structure. We believe it is possible to improve the quality of these particles by optimizing the plasma conditions. Finally, we have demonstrated that this single-step synthesis technique can be extended to other dielectric materials by simply changing the precursor gases flowing into the reactor.

ASSOCIATED CONTENT

Supporting Information

The Supporting Information is available free of charge at <https://pubs.acs.org/doi/10.1021/acs.nanolett.2c05084>.

Methods; plasma conditions for the synthesis of size-controlled c-Si NPs; plasma synthesis of high-index NPs other than Si; nonidealities of Si NPs of the 214 nm mean diameter sample; comparison of extinction measurements to extinction from a delta function size distribution (PDF)

AUTHOR INFORMATION

Corresponding Authors

Harry A. Atwater – Thomas J. Watson Laboratories of Applied Physics, California Institute of Technology, Pasadena, California 91125, United States; orcid.org/0000-0001-9435-0201; Email: haa@caltech.edu

Uwe R. Kortshagen – Department of Mechanical Engineering, University of Minnesota, Minneapolis, Minnesota 55455, United States; orcid.org/0000-0001-5944-3656; Email: kortshagen@umn.edu

Authors

Mohammad Ali Eslamisaray – Department of Mechanical Engineering, University of Minnesota, Minneapolis, Minnesota 55455, United States; orcid.org/0000-0001-8704-592X

Parker R. Wray – Department of Electrical Engineering, California Institute of Technology, Pasadena, California 91125, United States; orcid.org/0000-0003-3384-0826

Yeonjoo Lee – Department of Mechanical Engineering, University of Minnesota, Minneapolis, Minnesota 55455, United States; orcid.org/0000-0003-2096-5160

Gunnar M. Nelson – Department of Mechanical Engineering, University of Minnesota, Minneapolis, Minnesota 55455, United States

Ognjen Ilic – Department of Mechanical Engineering, University of Minnesota, Minneapolis, Minnesota 55455, United States; orcid.org/0000-0001-8651-7438

Complete contact information is available at: <https://pubs.acs.org/10.1021/acs.nanolett.2c05084>

Author Contributions

[†]M.A.E. and P.R.W. contributed equally. The manuscript was written through contributions of all authors. All authors have given approval to the final version of the manuscript.

Notes

The authors declare no competing financial interest.

ACKNOWLEDGMENTS

This work was supported by the Army Research Office under MURI project W911NF-18-1-0240. Portions of this work were conducted in the Minnesota Nano Center, which is supported by the National Science Foundation through the National Nanotechnology Coordinated Infrastructure (NNCI) under Award No. ECCS-2025124. Parts of this work were carried out in the Characterization Facility, University of Minnesota, which receives partial support from the NSF through the MRSEC (Award Number DMR-2011401) and the NNCI (Award Number ECCS-2025124) programs.

REFERENCES

- (1) Yu, P. Y.; Cardona, M. *Fundamentals of Semiconductors*; Graduate Texts in Physics; Springer: Berlin, 2010. DOI: [10.1007/978-3-642-00710-1](https://doi.org/10.1007/978-3-642-00710-1).
- (2) Baranov, D. G.; Zuev, D. A.; Lepeshov, S. I.; Kotov, O. V.; Krasnok, A. E.; Evlyukhin, A. B.; Chichkov, B. N. All-Dielectric Nanophotonics: The Quest for Better Materials and Fabrication Techniques. *Optica* **2017**, *4* (7), 814.
- (3) Khurgin, J. B. Expanding the Photonic Palette: Exploring High Index Materials. *ACS Photonics* **2022**, *9* (3), 743–751.
- (4) Kerker, M.; Wang, D.-S.; Giles, C. L. Electromagnetic Scattering by Magnetic Spheres. *J. Opt. Soc. Am.* **1983**, *73* (6), 765.
- (5) Liu, W.; Kivshar, Y. S. Generalized Kerker Effects in Nanophotonics and Meta-Optics [Invited]. *Opt. Express* **2018**, *26* (10), 13085.
- (6) Hasan, M. R.; Hellesø, O. G. Dielectric Optical Nanoantennas. *Nanotechnology* **2021**, *32* (20), 202001.
- (7) Kivshar, Y. All-Dielectric Meta-Optics and Non-Linear Nanophotonics. *Natl. Sci. Rev.* **2018**, *5* (2), 144–158.
- (8) Jahani, S.; Jacob, Z. All-Dielectric Metamaterials. *Nat. Nanotechnol.* **2016**, *11* (1), 23–36.
- (9) Khurgin, J. B. How to Deal with the Loss in Plasmonics and Metamaterials. *Nat. Nanotechnol.* **2015**, *10* (1), 2–6.
- (10) Boriskina, S. V.; Cooper, T. A.; Zeng, L.; Ni, G.; Tong, J. K.; Tsurimaki, Y.; Huang, Y.; Meroueh, L.; Mahan, G.; Chen, G. Losses in Plasmonics: From Mitigating Energy Dissipation to Embracing Loss-Enabled Functionalities. *Adv. Opt. Photonics* **2017**, *9* (4), 775.
- (11) West, P. R.; Ishii, S.; Naik, G. V.; Emani, N. K.; Shalae, V. M.; Boltasseva, A. Searching for Better Plasmonic Materials. *Laser Photonics Rev.* **2010**, *4* (6), 795–808.
- (12) Monticone, F.; Argyropoulos, C.; Alu, A. Optical Antennas: Controlling Electromagnetic Scattering, Radiation, and Emission at the Nanoscale. *IEEE Antennas Propag. Mag.* **2017**, *59* (6), 43–61.
- (13) Shim, H.; Monticone, F.; Miller, O. D. Fundamental Limits to the Refractive Index of Transparent Optical Materials. *Adv. Mater.* **2021**, *33* (43), 2103946.
- (14) Itagi, A. V.; Challener, W. A. Optics of Photonic Nanojets. *J. Opt. Soc. Am. A* **2005**, *22* (12), 2847.
- (15) Tzarouchis, D.; Sihvola, A. Light Scattering by a Dielectric Sphere: Perspectives on the Mie Resonances. *Appl. Sci.* **2018**, *8* (2), 184.

- (16) Shamkhi, H. K.; Sayanskiy, A.; Valero, A. C.; Kupriianov, A. S.; Kapitanova, P.; Kivshar, Y. S.; Shalin, A. S.; Tuz, V. R. Transparency and Perfect Absorption of All-Dielectric Resonant Metasurfaces Governed by the Transverse Kerker Effect. *Phys. Rev. Mater.* **2019**, *3* (8), 085201.
- (17) Fu, Y. H.; Kuznetsov, A. I.; Miroshnichenko, A. E.; Yu, Y. F.; Luk'yanchuk, B. Directional Visible Light Scattering by Silicon Nanoparticles. *Nat. Commun.* **2013**, *4* (1), 1527.
- (18) Alaei, R.; Filter, R.; Lehr, D.; Lederer, F.; Rockstuhl, C. A Generalized Kerker Condition for Highly Directive Nanoantennas. *Opt. Lett.* **2015**, *40* (11), 2645.
- (19) Achouri, K.; Caloz, C. *Electromagnetic Metasurfaces: Theory and Applications*; Wiley-IEEE Press: Hoboken, NJ, 2021.
- (20) Liu, S.; Sinclair, M. B.; Mahony, T. S.; Jun, Y. C.; Campione, S.; Ginn, J.; Bender, D. A.; Wendt, J. R.; Ihlefeld, J. F.; Clem, P. G.; Wright, J. B.; Brener, I. Optical Magnetic Mirrors without Metals. *Optica* **2014**, *1* (4), 250.
- (21) Chen, H.-T.; Taylor, A. J.; Yu, N. A Review of Metasurfaces: Physics and Applications. *Rep. Prog. Phys.* **2016**, *79* (7), 076401.
- (22) Tribelsky, M. I.; Flach, S.; Miroshnichenko, A. E.; Gorbach, A. V.; Kivshar, Y. S. Light Scattering by a Finite Obstacle and Fano Resonances. *Phys. Rev. Lett.* **2008**, *100* (4), 043903.
- (23) Utyushev, A. D.; Zakomirnyi, V. I.; Rasskazov, I. L. Collective Lattice Resonances: Plasmonics and Beyond. *Rev. Phys.* **2021**, *6*, 100051.
- (24) Tong, J.; Suo, F.; Tobing, L. Y. M.; Yao, N.; Zhang, D.; Huang, Z.; Zhang, D. H. High Order Magnetic and Electric Resonant Modes of Split Ring Resonator Metasurface Arrays for Strong Enhancement of Mid-Infrared Photodetection. *ACS Appl. Mater. Interfaces* **2020**, *12* (7), 8835–8844.
- (25) Bourgeois, M. R.; Rossi, A. W.; Chalifour, M.; Cherqui, C.; Masiello, D. J. Lattice Kerker Effect with Plasmonic Oligomers. *J. Phys. Chem. C* **2021**, *125* (34), 18817–18826.
- (26) Gerasimov, V. S.; Ershov, A. E.; Bikbaev, R. G.; Rasskazov, I. L.; Isaev, I. L.; Semina, P. N.; Kostyukov, A. S.; Zakomirnyi, V. I.; Polyutov, S. P.; Karpov, S. V. Plasmonic Lattice Kerker Effect in Ultraviolet-Visible Spectral Range. *Phys. Rev. B* **2021**, *103* (3), 035402.
- (27) Zhou, J.; Panday, A.; Xu, Y.; Chen, X.; Chen, L.; Ji, C.; Guo, L. J. Visualizing Mie Resonances in Low-Index Dielectric Nanoparticles. *Phys. Rev. Lett.* **2018**, *120* (25), 253902.
- (28) Wang, W.; Ma, X. Achieving Extreme Light Confinement in Low-Index Dielectric Resonators through Quasi-Bound States in the Continuum. *Opt. Lett.* **2021**, *46* (24), 6087.
- (29) Kuznetsov, A. I.; Miroshnichenko, A. E.; Fu, Y. H.; Zhang, J.; Luk'yanchuk, B. Magnetic Light. *Sci. Rep.* **2012**, *2* (1), 492.
- (30) García-Etxarri, A.; Gómez-Medina, R.; Froufe-Pérez, L. S.; López, C.; Chantada, L.; Scheffold, F.; Aizpurua, J.; Nieto-Vesperinas, M.; Sáenz, J. J. Strong Magnetic Response of Submicron Silicon Particles in the Infrared. *Opt. Express* **2011**, *19* (6), 4815.
- (31) Evlyukhin, A. B.; Novikov, S. M.; Zywiets, U.; Eriksen, R. L.; Reinhardt, C.; Bozhevolnyi, S. I.; Chichkov, B. N. Demonstration of Magnetic Dipole Resonances of Dielectric Nanospheres in the Visible Region. *Nano Lett.* **2012**, *12* (7), 3749–3755.
- (32) De Marco, M. L.; Semlali, S.; Korgel, B. A.; Barois, P.; Drisko, G. L.; Aymonier, C. Silicon-Based Dielectric Metamaterials: Focus on the Current Synthetic Challenges. *Angew. Chem., Int. Ed.* **2018**, *57* (17), 4478–4498.
- (33) Yan, J.; Liu, P.; Lin, Z.; Wang, H.; Chen, H.; Wang, C.; Yang, G. Directional Fano Resonance in a Silicon Nanosphere Dimer. *ACS Nano* **2015**, *9* (3), 2968–2980.
- (34) Li, C.-Q.; Zhang, C.-Y.; Huang, Z.-S.; Li, X.-F.; Dai, Q.-F.; Lan, S.; Tie, S.-L. Assembling of Silicon Nanoflowers with Significantly Enhanced Second Harmonic Generation Using Silicon Nanospheres Fabricated by Femtosecond Laser Ablation. *J. Phys. Chem. C* **2013**, *117* (46), 24625–24631.
- (35) Abderrafi, K.; García Calzada, R.; Gongalsky, M. B.; Suárez, I.; Abarques, R.; Chirvony, V. S.; Timoshenko, V. Yu.; Ibáñez, R.; Martínez-Pastor, J. P. Silicon Nanocrystals Produced by Nanosecond Laser Ablation in an Organic Liquid. *J. Phys. Chem. C* **2011**, *115* (12), 5147–5151.
- (36) Zywiets, U.; Evlyukhin, A. B.; Reinhardt, C.; Chichkov, B. N. Laser Printing of Silicon Nanoparticles with Resonant Optical Electric and Magnetic Responses. *Nat. Commun.* **2014**, *5* (1), 3402.
- (37) Zywiets, U.; Reinhardt, C.; Evlyukhin, A. B.; Birr, T.; Chichkov, B. N. Generation and Patterning of Si Nanoparticles by Femtosecond Laser Pulses. *Appl. Phys. A: Mater. Sci. Process.* **2014**, *114* (1), 45–50.
- (38) Fenollosa, R.; Meseguer, F.; Tymczenko, M. Silicon Colloids: From Microcavities to Photonic Sponges. *Adv. Mater.* **2008**, *20* (1), 95–98.
- (39) Shi, L.; Tuzer, T. U.; Fenollosa, R.; Meseguer, F. A New Dielectric Metamaterial Building Block with a Strong Magnetic Response in the Sub-1.5-Micrometer Region: Silicon Colloid Nanocavities. *Adv. Mater.* **2012**, *24* (44), 5934–5938.
- (40) Harris, J. T.; Hueso, J. L.; Korgel, B. A. Hydrogenated Amorphous Silicon (a-Si:H) Colloids. *Chem. Mater.* **2010**, *22* (23), 6378–6383.
- (41) Chaàbani, W.; Proust, J.; Movsesyan, A.; Béal, J.; Baudrion, A.-L.; Adam, P.-M.; Chehaidar, A.; Plain, J. Large-Scale and Low-Cost Fabrication of Silicon Mie Resonators. *ACS Nano* **2019**, *13* (4), 4199–4208.
- (42) Sugimoto, H.; Fujii, M. Colloidal Dispersion of Subquarter Micrometer Silicon Spheres for Low-Loss Antenna in Visible Regime. *Adv. Opt. Mater.* **2017**, *5* (17), 1700332.
- (43) Sugimoto, H.; Okazaki, T.; Fujii, M. Mie Resonator Color Inks of Monodispersed and Perfectly Spherical Crystalline Silicon Nanoparticles. *Adv. Opt. Mater.* **2020**, *8* (12), 2000033.
- (44) Mangolini, L.; Thimsen, E.; Kortshagen, U. High-Yield Plasma Synthesis of Luminescent Silicon Nanocrystals. *Nano Lett.* **2005**, *5* (4), 655–659.
- (45) Gresback, R.; Holman, Z.; Kortshagen, U. Nonthermal Plasma Synthesis of Size-Controlled, Monodisperse, Freestanding Germanium Nanocrystals. *Appl. Phys. Lett.* **2007**, *91* (9), 093119.
- (46) Wang, C.; Li, D.; Lu, Z.; Song, M.; Xia, W. Synthesis of Carbon Nanoparticles in a Non-Thermal Plasma Process. *Chem. Eng. Sci.* **2020**, *227*, 115921.
- (47) Lin, P. A.; Sankaran, R. M. Plasma-Assisted Dissociation of Organometallic Vapors for Continuous, Gas-Phase Preparation of Multimetallic Nanoparticles. *Angew. Chem., Int. Ed.* **2011**, *50* (46), 10953–10956.
- (48) Kumar, A.; Kang, S.; Larriba-Andaluz, C.; Ouyang, H.; Hogan, C. J.; Sankaran, R. M. Ligand-Free Ni Nanocluster Formation at Atmospheric Pressure via Rapid Quenching in a Microplasma Process. *Nanotechnology* **2014**, *25* (38), 385601.
- (49) Beaudette, C. A.; Andaraarachchi, H. P.; Wu, C.-C.; Kortshagen, U. R. Inductively Coupled Nonthermal Plasma Synthesis of Aluminum Nanoparticles. *Nanotechnology* **2021**, *32* (39), 395601.
- (50) Xu, C.; Andaraarachchi, H. P.; Xiong, Z.; Eslamisaray, M. A.; Kushner, M. J.; Kortshagen, U. R. Size-Tunable Silver Nanoparticle Synthesis in Glycerol Driven by a Low-Pressure Nonthermal Plasma. *J. Phys. Appl. Phys.* **2022**, *55* (1), 015201.
- (51) Rowe, D. J.; Kortshagen, U. R. Boron- and Phosphorus-Doped Silicon Germanium Alloy Nanocrystals—Nonthermal Plasma Synthesis and Gas-Phase Thin Film Deposition. *APL Mater.* **2014**, *2* (2), 022104.
- (52) Coleman, D.; Lopez, T.; Yasar-Inceoglu, O.; Mangolini, L. Hollow Silicon Carbide Nanoparticles from a Non-Thermal Plasma Process. *J. Appl. Phys.* **2015**, *117* (19), 193301.
- (53) Greenberg, B. L.; Ganguly, S.; Held, J. T.; Kramer, N. J.; Mkhoyan, K. A.; Aydil, E. S.; Kortshagen, U. R. Nonequilibrium-Plasma-Synthesized ZnO Nanocrystals with Plasmon Resonance Tunable via Al Doping and Quantum Confinement. *Nano Lett.* **2015**, *15* (12), 8162–8169.
- (54) Alvarez Barragan, A.; Ilawe, N. V.; Zhong, L.; Wong, B. M.; Mangolini, L. A Non-Thermal Plasma Route to Plasmonic TiN Nanoparticles. *J. Phys. Chem. C* **2017**, *121* (4), 2316–2322.
- (55) Beaudette, C. A.; Tu, Q.; Eslamisaray, M. A.; Kortshagen, U. R. Plasma-Synthesized Nitrogen-Doped Titanium Dioxide Nanoparticles

With Tunable Visible Light Absorption and Photocatalytic Activity. *ASME Open J. Eng.* **2022**, *1*, 011010.

(56) Kortshagen, U. R.; Sankaran, R. M.; Pereira, R. N.; Girshick, S. L.; Wu, J. J.; Aydil, E. S. Nonthermal Plasma Synthesis of Nanocrystals: Fundamental Principles, Materials, and Applications. *Chem. Rev.* **2016**, *116* (18), 11061–11127.

(57) Yasar-Inceoglu, O.; Lopez, T.; Farshihagro, E.; Mangolini, L. Silicon Nanocrystal Production through Non-Thermal Plasma Synthesis: A Comparative Study between Silicon Tetrachloride and Silane Precursors. *Nanotechnology* **2012**, *23* (25), 255604.

(58) Mangolini, L.; Kortshagen, U. Plasma-Assisted Synthesis of Silicon Nanocrystal Inks. *Adv. Mater.* **2007**, *19* (18), 2513–2519.

(59) Li, Z.; Kortshagen, U. R. Aerosol-Phase Synthesis and Processing of Luminescent Silicon Nanocrystals. *Chem. Mater.* **2019**, *31* (20), 8451–8458.

(60) Firth, P.; Holman, Z. C. Aerosol Impaction-Driven Assembly System for the Production of Uniform Nanoparticle Thin Films with Independently Tunable Thickness and Porosity. *ACS Appl. Nano Mater.* **2018**, *1* (8), 4351–4357.

(61) Bapat, A.; Anderson, C.; Perrey, C. R.; Carter, C. B.; Campbell, S. A.; Kortshagen, U. Plasma Synthesis of Single-Crystal Silicon Nanoparticles for Novel Electronic Device Applications. *Plasma Phys. Control. Fusion* **2004**, *46* (12B), B97–B109.

(62) Wray, P. R.; Eslamisaray, M. A.; Nelson, G. M.; Ilic, O.; Kortshagen, U. R.; Atwater, H. A. Broadband, Angle- and Polarization-Invariant Antireflective and Absorbing Films by a Scalable Synthesis of Monodisperse Silicon Nanoparticles. *ACS Appl. Mater. Interfaces* **2022**, *14* (20), 23624–23636.

(63) Kramer, N. J.; Anthony, R. J.; Mamunuru, M.; Aydil, E. S.; Kortshagen, U. R. Plasma-Induced Crystallization of Silicon Nanoparticles. *J. Phys. Appl. Phys.* **2014**, *47* (7), 075202.

(64) Xiong, Z.; Lanham, S.; Husmann, E.; Nelson, G.; Eslamisaray, M. A.; Polito, J.; Liu, Y.; Goree, J.; Thimsen, E.; Kushner, M. J.; Kortshagen, U. R. Particle Trapping, Size-Filtering, and Focusing in the Nonthermal Plasma Synthesis of Sub-10 Nanometer Particles. *J. Phys. Appl. Phys.* **2022**, *55* (23), 235202.

(65) Ledoux, G.; Guillois, O.; Porterat, D.; Reynaud, C.; Huisken, F.; Kohn, B.; Paillard, V. Photoluminescence Properties of Silicon Nanocrystals as a Function of Their Size. *Phys. Rev. B* **2000**, *62* (23), 15942–15951.

(66) Winters, B. J.; Holm, J.; Roberts, J. T. Thermal Processing and Native Oxidation of Silicon Nanoparticles. *J. Nanoparticle Res.* **2011**, *13* (10), 5473–5484.

(67) Perrey, C. R.; Carter, C. B. Insights into Nanoparticle Formation Mechanisms. *J. Mater. Sci.* **2006**, *41* (9), 2711–2722.